Scattering halos in strongly interacting Feshbach molecular Bose-Einstein condensates

Yuying Chen [1,*] Zhengxi Zhang,[2,*] Chi-Kin Lai [2] Yun Liang [2] Hongmian Shui,[2,3]
Haixiang Fu,[4] Fansu Wei [2,†] and Xiaoji Zhou [2,3,‡]

[1]*School of Physics and Electronics Engineering, Shanxi University, Taiyuan 030006, China*
[2]*State Key Laboratory of Photonics and Communications, School of Electronics, Peking University, Beijing 100871, China*
[3]*Institute of Carbon-Based Thin Film Electronics, Peking University, Shanxi, Taiyuan 030012, China*
[4]*College of Information Science and Engineering, Huaqiao University, Xiamen, Fujian 361021, China*

(Received 23 December 2024; accepted 25 March 2025; published 3 April 2025)

We investigate the scattering halos resulting from collisions between discrete momentum components in the time-of-flight expansion of interaction-tunable $^6Li_2$ molecular Bose-Einstein condensates. A key highlight of this study is the observation of the influence of interactions on the collisional scattering process. We measure the production of scattering halos at different interaction levels by varying the number of particles and the scattering length, and quantitatively assess the applicability of perturbation theory. To delve into a general theory of scattering halos, we introduce a scattering factor and obtain a universal relation between it and the halo ratio. Furthermore, we simulate the formation of scattering halos under nonperturbative conditions and discuss the contribution of in-trap dynamics to the scattering halos through a return pulse experiment. This study enhances our understanding of the physical mechanisms underlying scattering processes in many-body systems and provides new perspectives for further theoretical research.

DOI: 10.1103/PhysRevA.111.043303

I. INTRODUCTION

Among the fundamental interaction phenomena within many-body systems, collisional scattering stands out as a key process with abundant mechanisms [1–3]. The advent of laser cooling has made it possible to explore quantum many-body effects in cold atomic and molecular systems [4–8], spawning numerous theoretical and experimental studies of low-energy collisions [9–11]. Of particular significance are seminal experiments observing velocity-dependent collision suppression in Bose condensates [12], which demonstrated the Landau criterion for superfluidity through impurity atom propagation and bosonic collision enhancement. Meanwhile, recent advances in lattice systems [13] established quantitative models for *s*-wave scattering halos during time-of-flight (TOF) [14] expansion, validating ballistic expansion assumptions through classical collision theory. These developments highlighted the scattering halo's indispensable role in probing quantum dynamics [15–17].

The application of optical lattices to quantum gases greatly enriches the means of manipulation [18,19]. Due to their high controllability, they offer powerful and versatile experimental methods for exploring novel quantum states [20–22], high-precision metrology [23–25], quantum computing [26], and other quantum simulations [21,27–29]. Optical lattice pulses can rapidly modulate the external states of particles to prepare multiple discrete momentum components [17,30]. They are separated during TOF expansion, allowing the direct observation of transport, interference, and collisional scattering between them.

In ultracold gases, collisional scattering halos have revealed rich physics through velocity-dependent studies [12,31,32], multiparticle correlations [33,34], quantum thermalization [35], entanglement dynamics [36,37], and ghost imaging within the field of quantum optics [38]. While recent work [13] achieved quantitative modeling of lattice system collisions under moderate interactions, existing studies remain limited to weak coupling regimes with sparse halos [17,39–41]. To date, there have been no experiments to study the collisional scattering processes under strong interactions.

In this work, we investigate the collisional scattering halos between discrete momentum components of $^6Li_2$ molecular Bose-Einstein condensates (mBECs) produced by one-dimensional (1D) lattice pulses during the TOF process. Experimentally, we study the impact of interactions on the scattering halos N_{sc} over a wide range by varying the *s*-wave scattering length a_s and the number of total particles N_0. The scattering length is directly modulated by a Feshbach magnetic field [42–45], and the number of condensed particles is controlled by the loading time of the magnetooptical trap (MOT). Theoretically, we use perturbation theory to quantitatively explain the changes in the scattering halos and identify their validity in different interaction regions. A scattering factor γ is introduced to derive a universal relation with the halo ratio P_{sc} in the experiment. Consequently, for comparison with the experiments, we study the changes in scattering halos by numerical simulations under nonperturbative conditions and conduct a return pulse experiment to discuss the contribution of in-trap dynamics to the scattering halos.

*These authors contributed equally to this work.
†Contact author: wfs@pku.edu.cn
‡Contact author: xjzhou@pku.edu.cn

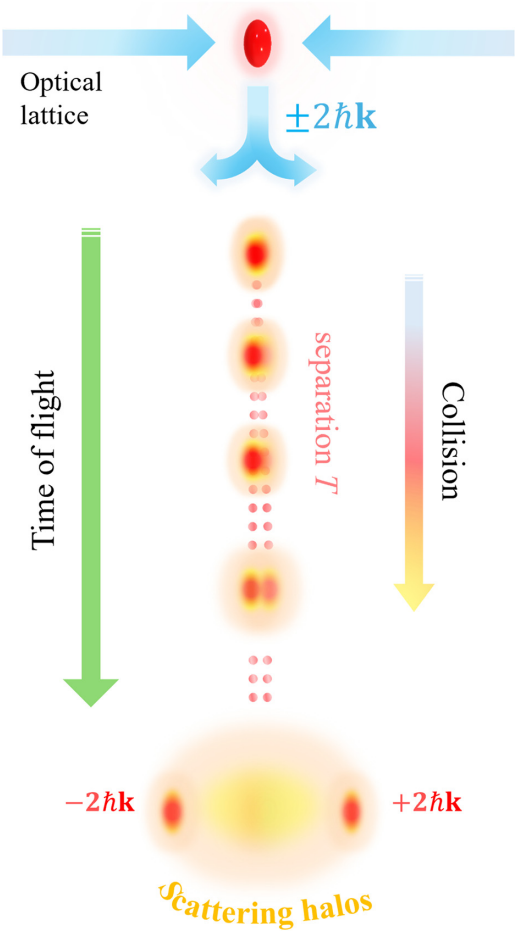

FIG. 1. Scheme of the experimental design. The $^6Li_2$ molecular Bose-Einstein condensates (red particle clouds), pulsed by a 1D optical lattice (blue arrows), expand into free space after the lattice beams and trapping potential are instantaneously turned off. Due to the designed lattice pulses, a 50:50 proportion of $\pm 2\hbar k$ momentum modes is formed. They pass through each other during the separation time T in the TOF, leading to elastic two-body collisions. After this, the scattering halo (light yellow halos) will emerge between the two momentum peaks.

This paper is organized as follows. In Sec. II, we describe our experimental implementation. In Sec. III, the classical model of collision for scattering halos in a 1D optical lattice with strong interaction strength is described. In Sec. IV, we present the experimental results of scattering halos with different interactions. Finally, we give the conclusion in Sec. V.

II. EXPERIMENTAL IMPLEMENTATION

A. Experimental design

The overall experimental design is shown in Fig. 1. We design 1D lattice pulses by the shortcut method (see Appendix A for details) [21,46,47] to load the molecular Bose-Einstein condensate (mBEC) from state $|\psi_0\rangle = |p = 0\rangle$ into state $|\psi\rangle = \frac{1}{\sqrt{2}}(|p = +2\hbar k\rangle + |p = -2\hbar k\rangle)$, where p is the momentum, $\hbar$ is the reduced Planck's constant, $k = \pi/D$ is the wave vector of the optical lattice, and D is the lattice constant. After the state preparation, the lattice beams and trapping potential are turned off instantaneously, and the particles with different momentum modes that initially overlap each other in space will separate. The total time required for the separation of particles with different momenta $+2\hbar k$ and $-2\hbar k$ is denoted by T, in which elastic two-body collisions occur and produce a scattering halo between the two momentum peaks. The entire process is visualized through TOF absorption imaging.

The formation of scattering halos is closely related to the interaction strength. For a trapped condensate, the interaction strength is positively correlated with s-wave scattering length a_s and particle density n. With different a_s and n, the scattering halos formed during TOF are also different.

B. Experimental setup and sequence

We first prepare a two-component mixture of ^{6}Li atoms in their lowest hyperfine states: $|1\rangle = |F = 1/2, m_F = 1/2\rangle$, and $|2\rangle = |F = 1/2, m_F = -1/2\rangle$. Through evaporative cooling in an optical dipole trap at 810 Gauss near the Feshbach resonance, followed by magnetic-field tuning to the BEC regime (ranging from 655 to 766 Gauss in our experiment), we obtain pure $^6Li_2$ mBECs with minimal thermal background. The total particle number N_0 is controlled by adjusting the MOT loading time (from 1 s to 8 s), yielding $N_0 = 1 \times 10^3$ to 5×10^4, while maintaining fixed trap frequencies. The intermolecular s-wave scattering length a_s is tuned via the Feshbach field as $a_s = 0.6a_{12}$ [9], where a_{12} denotes the atomic scattering length between states $|1\rangle$ and $|2\rangle$. In this work, a_s spans $865a_0$ to $2623a_0$ ($a_0 = 0.0529$ nm), enabling the exploration of strongly interacting regimes. As detailed in our prior work [48], the mBEC is confined in a crossed optical dipole trap formed by two far-red-detuned laser beams intersecting at 30° in the vertical x-z plane [Fig. 2(a)]. The resulting trapping frequencies are $(\omega_x, \omega_y, \omega_z) = 2\pi \times (39.5, 200, 200)$ Hz. The 1D optical lattice, whose lattice constant $D = \lambda/2 = 532$ nm, is composed of a $\lambda = 1064$ nm laser beam and retroreflected beam. The characteristic lattice energy is $E_r = \hbar^2k^2/2m$, where $k = \pi/D$ and m is the mass of a lithium molecule ($^6Li_2$). The lattice beam intensity is controlled by an acoustooptic modulator (AOM) with feedback control, and another AOM is used for a synchronous on-off radio frequency (RF) switch.

Figure 2(b) illustrates the experimental time sequence. The process begins with the mBEC preparation: we ramp the Feshbach magnetic field from B_i to B_f over t_{shift}, maintaining B_f for $t_{\text{hold}} = 100$ ms to stabilize the condensate. In the second stage, we employ a shortcut lattice pulsing technique to populate discrete momentum states. For a lattice depth $V_0 = 10E_r$, we apply a two-pulse sequence with timings $(t_1^{\text{on}}, t_1^{\text{off}}, t_2^{\text{on}}, t_2^{\text{off}}) = (12.3, 6.8, 7.1, 18.2)$ μs, achieving 99.9% theoretical fidelity in the noninteracting limit (see Table I in Appendix A for details) [46]. Crucially, this method preserves high fidelity across interaction regimes. Following TOF expansion ($t_{\text{TOF}} = 2$ ms), a 20-μs probe pulse captures absorption images for momentum distribution analysis. Figure 2(c) displays representative images at $a_s = 865a_0$ and $1600a_0$. We extract 1D density profiles along the lattice axis [y integration, Fig. 2(c), bottom] to quantify the total particle number N_0 through spatial integration. A bimodal fit

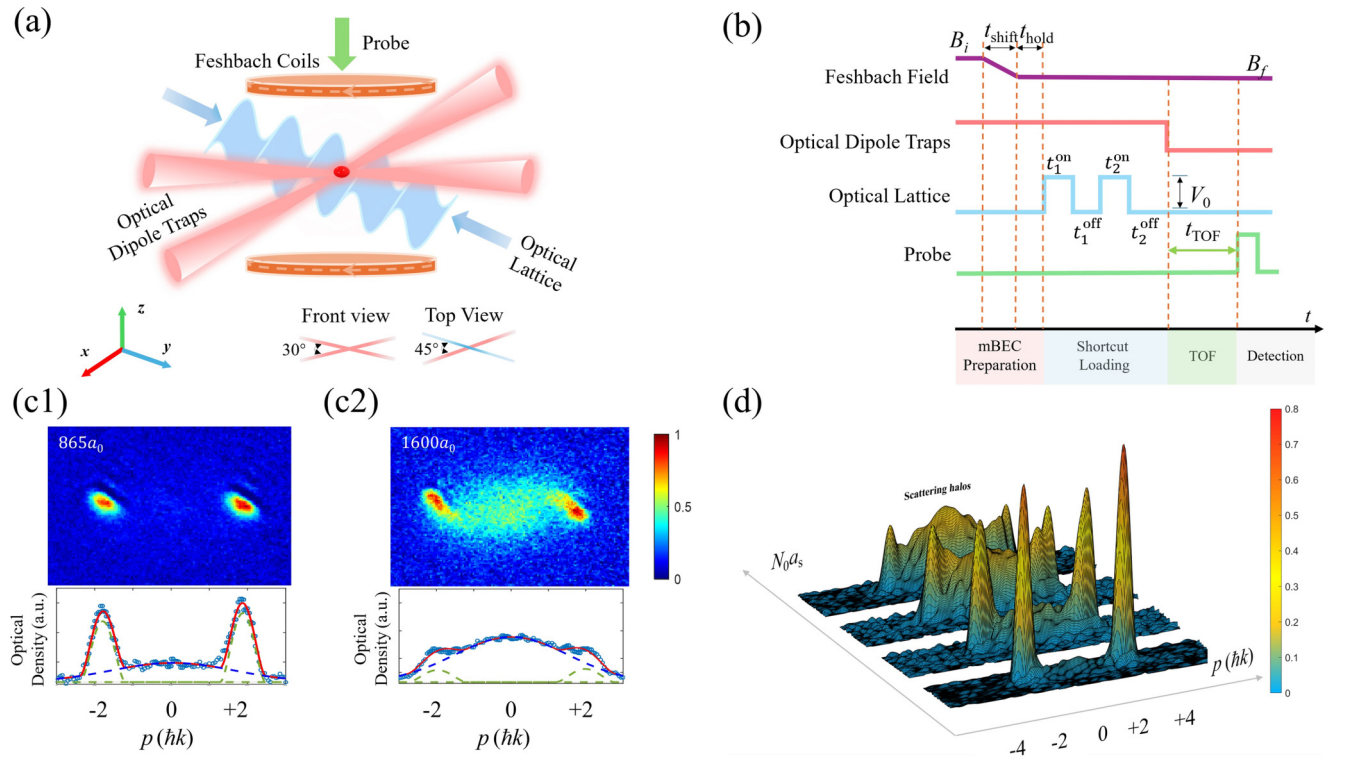

FIG. 2. (a) Schematic of the experimental system. The brown circles in the x-y plane represent the Feshbach magnetic coils. Feshbach mBECs are trapped in a pair of crossed optical dipole traps at 30° to each other in the y-z plane (front view). The two blue arrows in the x-y plane represent the lattice beams, which form a 45° angle with the optical trap (top view). The green arrow shows the imaging direction, which is perpendicular to the x-y plane. (b) A typical experimental time sequence. The horizontal axis denotes the experimental time. The purple line and red line represent the Feshbach field and optical dipole trap, respectively. The Feshbach field is switched from B_i to B_f in $t_{\rm shift}$ and kept for a period of $t_{\rm hold} = 100$ ms. The blue line represents the optical lattice. Several shortcut pulses $t_i^{\rm on(off)}$ are designed to load mBEC into the different momentum states $\pm 2\hbar k$ with lattice depth $V_0 = 10E_r$. The green line represents the probe beam with duration time 20 μs, which is applied after the time-of-flight process with time $t_{\rm TOF} = 2$ ms. Different stages are marked at the bottom with varying colors. Panel (c) corresponds to scattering patterns for different scattering strengths of (c1) $850a_0$ and (c2) $1600a_0$, with a fixed number of total particles N_0 approximately equal to 2×10^4. The corresponding curves below the images are obtained by integrating along the y direction, showing the bimodal fitting result for distinguishing between the condensed (the green dashed line) and noncondensed (the blue dashed line) part, and the light blue circles represent experimental results. The horizontal axis represents the momentum p. (d) A stereoscopic view of the two-dimensional particle momentum distribution observed through absorption imaging after a certain time of flight. The x axis of the horizontal plane coordinate represents different momentum states, and the y axis represents the interaction strength (quantified jointly by the number of mBEC N_0 and the scattering length a_s). The color scale denotes the normalized density of particles.

distinguishes condensed (green dashed) and thermal (blue dashed) fractions, with the latter defining the scattering halo population $N_{\rm sc}$. This enables the systematic comparison of the scattering halo formation across interaction strengths.

Our measurements reveal a pronounced interaction dependence: stronger interactions couplings ($1600a_0$) generate significantly enhanced halos compared to $865a_0$. Figure 2(d) provides a stereoscopic perspective of the two-dimensional particle distribution across various interactions after a definite TOF. To disentangle density and interaction effects, we systematically vary both a_s (via Feshbach tuning) and N_0 (controlled by MOT loading time), establishing $N_{\rm sc}$ as a direct metric for halo formation dynamics.

III. PERTURBATION THEORY OF SCATTERING HALOS

To interpret the experimental observations, we develop a theoretical framework based on first-order perturbation theory, which models halo formation via classical collisions [11,15,16]. The scattering rate of particles into the halo is governed by

$$\frac{\mathrm{d}}{\mathrm{d}t}N_{\rm sc} = 2\int d\vec{r}\,\sigma n_+(\vec{r},t)n_-(\vec{r},t)v, \tag{1}$$

where $\sigma = 8\pi a_s^2$ is the s-wave cross section, $n_\pm(\vec{r},t)$ represent the densities of the $\pm 2\hbar k$ momentum components, and $v = 4\hbar k/m$ is the relative velocity induced by the optical lattice pulses. The collision rate $\Gamma = \sigma n_+ n_- v$ quantifies the number of collisions per unit time at position $\vec{r}$ and time t. This perturbative treatment assumes negligible feedback from scattered halo particles, approximating $n_\pm(\vec{r},t) \approx n_\pm(\vec{r} \mp \frac{1}{2}\vec{v}t, 0)$.

By using the Thomas-Fermi distribution and integrating Eq. (1) over the separation timescale T (Fig. 1), the total scattered particle number becomes

$$N_{\rm sc} = 8\pi\epsilon\left(\frac{a_s N_0}{R}\right)^2 \propto (a_s N_0)^{8/5}, \tag{2}$$

where $\epsilon = 0.102$ accounts for trap anisotropy (see Appendix B for details), and the Thomas-Fermi radius R [13,49] is

$$R = (15N_0 a_s \bar{a}^4)^{1/5}, \tag{3}$$

where $\bar{a} = [\hbar/(m\bar{\omega})]^{1/2}$ and $\bar{\omega} = (\omega_x\omega_y\omega_z)^{1/3}$.

The validity of this model depends critically on the dimensionless scattering factor

$$\gamma = \frac{N_{\rm sc}}{N_0} = 8\pi\epsilon\frac{a_s^2 N_0}{R^2}, \tag{4}$$

derived from Eq. (2). Physically, $\gamma \sim \sigma n R \sim \Gamma T$ represents the cumulative scattering probability during TOF, combining scattering length (a_s), density (N_0/R^2), and system parameters (ϵ).

When $\gamma \ll 1$ (e.g., as $a_s \lesssim 100a_0$, $N_0 \lesssim 10^5$), the perturbative theory aligns well with experimental results [13]. Nevertheless, in our strongly interacting regime (as $a_s \geqslant 865a_0$, $N_0 > 10^4$), discrepancies emerge due to the dynamical feedback from halo particles. Specifically, nonperturbative scattering occurs as the increase in a_s and N_0 boosts the halo density $n_{\rm sc}$, leading to the involvement of scattered particles in collisions. Moreover, the effective $n_{\pm}(\vec{r}, t)$ distributions deviate from their initial forms with the growth of halo-mediated collisions, further modifying the density evolution.

IV. EXPERIMENTAL RESULTS AND ANALYSIS

Based on the experimental protocol outlined in Sec. II, we systematically measure the scattered halo population $N_{\rm sc}$ and the halo ratio $P_{\rm sc} = N_{\rm sc}/N_0$ (defined as the fraction of scattered particles) across a wide parameter space. By independently tuning the s-wave scattering length ($a_s = 865a_0$, $1600a_0$, $2004a_0$, $2623a_0$) and the total particle number ($N_0 = 1 \times 10^3$ to 5×10^4), we map the interplay between the interaction strength and halo formation (Fig. 3). In Sec. IV A, we compare these measurements with perturbation theory predictions to quantify the regime of validity. In Sec. IV B, the introduction of a dimensionless scattering factor γ [Eq. (4)] is parameterized the scattering probability during TOF. Through analysis, we obtain a universal scaling relation $P_{\rm sc} = f(\gamma)$. In Sec. IV C, we correct the results for the nonperturbative case through numerical simulations. Finally, Sec. IV D discusses the contributions of in-trap versus TOF dynamics to the scattered halo particle number via controlled return-pulse experiments.

A. Effect of interactions on the particle number of halos

Figure 3(a) presents the experimental dependence of the scattered halo population $N_{\rm sc}$ on the total particle number N_0 for different scattering lengths a_s, plotted on a logarithmic scale. The colored dashed lines denote the perturbation theory predictions [Eq. (2)], which exhibit a characteristic power-law slope of 8/5 after logarithmic transformation. When a_s is held constant, the experimental data reveal a gradual deviation from linearity in the log-log plot as N_0 increases. At low N_0, the measurements align closely with the theoretical curves. However, for larger N_0, the data increasingly diverge from these predictions: the slope of $N_{\rm sc}$ versus N_0 decreases systematically from 8/5 toward unity, and all datasets converge toward a universal cyan line ($N_{\rm sc} = N_0$). This saturation behavior signifies that nearly all particles undergo scattering at high N_0, consistent with a fully depleted condensate.

To further illustrate the $N_{\rm sc}$-a_s relationship, we analyze three distinct particle numbers ($N_0 \approx 2.1 \times 10^3$, 5.1×10^3, and 1.1×10^4; uncertainty = 5%), as shown in Fig. 3(b). The hollow blue markers represent experimental data, while the dashed lines correspond to perturbation theory predictions. For $N_0 \approx 2.1 \times 10^3$, the measured $N_{\rm sc}$ values match the theoretical curves across all a_s, confirming the validity of perturbation theory. In contrast, at higher N_0 (5.1×10^3 and 1.1×10^4), significant deviations emerge as a_s increases. These deviations evolve from partial disagreement to a complete breakdown of the perturbative framework, highlighting its inability to describe halo formation under strong interactions.

Collectively, these results demonstrate the limitations of perturbation theory in quantifying interaction-driven halo dynamics. While the theory successfully predicts $N_{\rm sc}$ at low a_s and N_0, its accuracy diminishes sharply in the strongly interacting regime. This necessitates theoretical refinements to account for nonlinear effects and many-body correlations.

B. Universal characterization of scattering halos

As shown in Fig. 3(c), the scattering halo ratio $P_{\rm sc} = N_{\rm sc}/N_0$ (defined as the ratio of scattered halo particles $N_{\rm sc}$ to the total initial particle number N_0) exhibits distinct experimental trends as a function of N_0 for different a_s values. To ensure statistical reliability, each data point represents the average of five independent measurements, with vertical error bars indicating the standard error of $P_{\rm sc}$ and horizontal error bars reflecting the standard deviation of N_0. While the experimental results agree well with theoretical predictions at low N_0, systematic deviations emerge as N_0 increases, manifesting as an overestimation of $P_{\rm sc}$ by the theory. Notably, the critical N_0 value marking the onset of this deviation shows a clear dependence on a_s, providing direct evidence of the coupled role of particle number and scattering length in halo formation.

To address the limitations of perturbation theory in describing the scattering halo, we introduce a scattering factor γ, as discussed in Sec. III. By analyzing the relationship between $P_{\rm sc}$ and γ, we uncover a universal scaling $P_{\rm sc} = f(\gamma)$, shown in Fig. 3(d). The inset highlights the $\gamma < 1$ regime, where the perturbative prediction (cyan curve) retains a linear dependence on γ. Despite variations in the experimental N_0 ranges for different a_s, all data collapse onto a single master curve when plotted against γ. This universal scaling resolves the apparent discrepancies in Fig. 3(c) and confirms the effectiveness of γ in capturing the interplay between a_s and N_0. A detailed analysis of the nonperturbation cases associated with $f(\gamma)$, including theoretical refinements and numerical simulations, will be presented in Sec. IV C.

C. Simulation for the nonperturbative case

To address the limitations of perturbation theory, we numerically simulate the scattering process using a modified

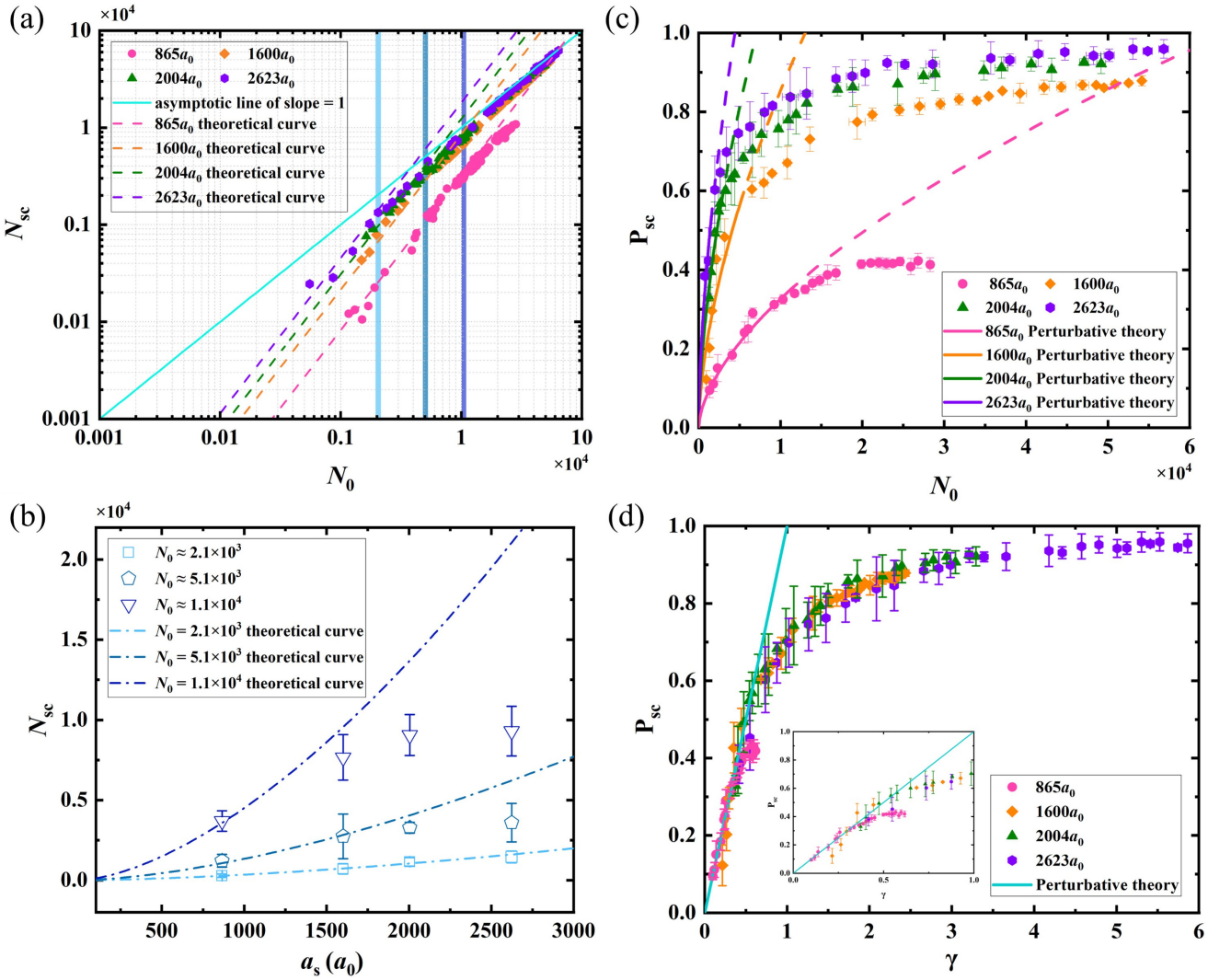

FIG. 3. The effect of interactions on scattering halos. (a) The particle number of halo N_{sc} with various total particle numbers N_0 in a logarithmic coordinate system. The pink circles, yellow diamonds, green triangles, and purple hexagons represent the experimental data for scattering lengths $a_s = 865a_0, 1600a_0, 2004a_0$, and $2623a_0$, respectively. The corresponding colored dashed lines are the perturbation theoretical curves. The cyan solid line indicates the benchmark line with a slope of 1. Three vertical bands indicate different total particle numbers corresponding to $N_0 \approx 2.1 \times 10^3$ (light blue), 5.1×10^3 (blue), and 1.1×10^4 (dark blue), with an uncertainty of 5% for the particle number ranges. (b) The relationship between the number of scattering halos N_{sc} and different scattering lengths a_s at various total particle numbers N_0. The light blue squares, blue pentagons, and dark blue triangles mark the experimental data of $N_0 \approx 2.1 \times 10^3$, 5.1×10^3, 1.1×10^4, and the dashed lines represent corresponding the perturbation theoretical curves. Error bars indicate the standard error of five measurements. (c) The relationship between the scattering halo ratio P_{sc}, which is the ratio of N_{sc} to the total particle number N_0, and the total particle number N_0. The lines of different styles correspond to the perturbation theoretical curves for different scattering lengths a_s. The experimental results are the average results of five measurements, and the corresponding error bars represent the uncertainty. (d) By analyzing the experimental data, we introduce the scattering factor γ and obtain a universal relationship between the scattering halo ratio P_{sc} and the γ. The inset highlights the region where $\gamma < 1$. The cyan curve represents predictions from perturbation theory. The corresponding error bars represent the uncertainty of P_{sc}.

equation

$$\frac{\mathrm{d}}{\mathrm{d}t}N_{sc} = \int \mathrm{d}\vec{r}\,\sigma\left[2vn_+(\vec{r},t)n_-(\vec{r},t) + \int n_+(\vec{r},t)n_{sc}(\vec{r},t,\vec{u})\left|\frac{1}{2}\vec{v}-\vec{u}\right|d\vec{u} + \int n_-(\vec{r},t)n_{sc}(\vec{r},t,\vec{u})\left|-\frac{1}{2}\vec{v}-\vec{u}\right|d\vec{u}\right]. \quad (5)$$

Among them, $n_{sc}(\vec{r},t,\vec{u})$ represents the phase-space density of the scattering halo at position $\vec{r}$ at time t with velocity $\vec{u}$. This equation extends the perturbation model [Eq. (1)], incorporating collisions between condensed particles and scattered particles.

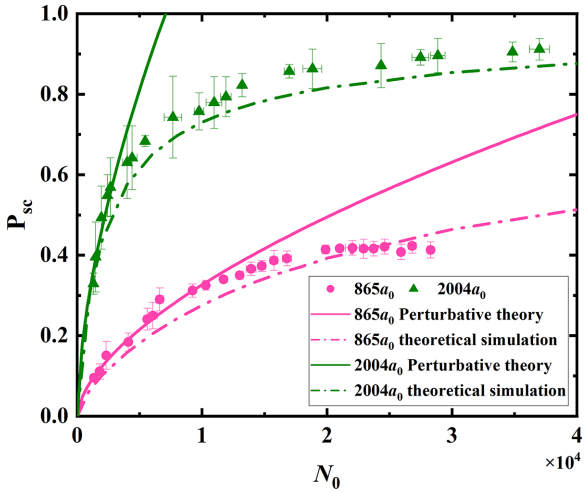

FIG. 4. Comparative analysis of numerical simulations and perturbation theory for the halo ratio P_{sc} as a function of the particle number N_0. The corresponding scattering lengths are $a_s = 865a_0$ (the pink circles) and $2004a_0$ (the green triangles), with solid lines representing the perturbation theoretical curves and dashed lines representing the numerical simulation curves.

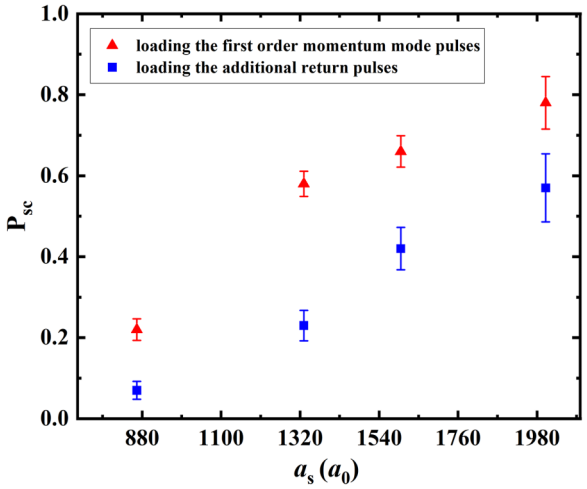

FIG. 5. Analysis of the variation in the noncondensed halo ratio at different stages of pulse loading, with a fixed particle number of 1.4×10^4, as the scattering length a_s changes. The experimental data after loading the first-order momentum lattice pulse is represented by red triangles, and the data after applying a return lattice pulse following the first-order momentum lattice pulse are represented by blue squares. Error bars indicate the standard error of five measurements.

By accounting for the reduction in the density of condensed particles (n_+ and n_-), the calculation of the density of scattered halo particles (n_{sc}) can be written as

$$\begin{aligned}
\frac{\mathrm{d}}{\mathrm{d}t}n_+(\vec{r},t) =& -\sigma v n_+(\vec{r},t)n_-(\vec{r},t) \\
&- \int \sigma n_+(\vec{r},t)n_{sc}(\vec{r},t,\vec{u})|\frac{1}{2}\vec{v}-\vec{u}|d\vec{u}, \\
\frac{\mathrm{d}}{\mathrm{d}t}n_-(\vec{r},t) =& -\sigma v n_-(\vec{r},t)n_+(\vec{r},t) \\
&- \int \sigma n_-(\vec{r},t)n_{sc}(\vec{r},t,\vec{u})|-\frac{1}{2}\vec{v}-\vec{u}|d\vec{u}, \\
\frac{\mathrm{d}}{\mathrm{d}t}n_{sc}(\vec{r},t) =& -\frac{\mathrm{d}}{\mathrm{d}t}n_+(\vec{r},t) - \frac{\mathrm{d}}{\mathrm{d}t}n_-(\vec{r},t). \qquad (6)
\end{aligned}$$

In the revised calculation of collision processes between condensed particles and scattered halo particles, we take into account the motion of condensed particles and the diffusion of the scattering halo. It is assumed that condensed particles with momenta of $\pm 2\hbar k$ (denoted as n_+ and n_-) retain their initial velocity $\pm v/2$. For halo particles generated through collisions between condensed particles, the calculation of their initial velocity distribution follows the kinematics of s-wave scattering [15], and subsequent collisions are neglected, meaning that this part can be treated as free diffusion.

By using Eqs. (5) and (6), we simulate the scattering process for different initial particle numbers N_0 at scattering lengths $a_s = 865a_0$ and $2004a_0$. We analyze the relationship between the halo ratio P_{sc} and N_0, comparing it with perturbation theory and experimental data. The parameters used in the simulation are consistent with experimental conditions, and we assume isotropic spreading of the scattering halo during TOF.

As shown in Fig. 4, the solid lines represent the results of Eq. (2), while the dashed lines show the simulation results based on Eq. (5). The triangular and circular dots indicate the experimental results for $865a_0$ and $2004a_0$, respectively [consistent with Fig. 3(c)]. When $\gamma < 1$, the experimental results align well with both the solid and dashed lines. Due to the decrease in the number of total particles during the TOF process, the simulation and experimental results are both lower than the perturbation theoretical curves. For the same particle number N_0, the deviation between experimental and simulation results is larger at $2004a_0$ than at $865a_0$, reflecting the reduced applicability of Eq. (2) at higher γ. This discrepancy likely arises from the semi-classical approximations in the simulation, experimental uncertainties, deviations from the ideal initial condensate ratio, and unaccounted scattering events during optical lattice pulses.

D. Discussion about in-trap dynamics

To evaluate the contribution of in-trap dynamics to the scattering halo, we design a return pulse experiment [50,51]. The experimental protocol begins by initializing the system in the first-order momentum order superposition state $|\psi\rangle = \frac{1}{\sqrt{2}}(|p = +2\hbar k\rangle + |p = -2\hbar k\rangle)$, followed by a tailored lattice pulse sequence $(t_{r1}^{\mathrm{on}}, t_{r1}^{\mathrm{off}}, t_{r2}^{\mathrm{on}}, t_{r2}^{\mathrm{off}}) = (19.3, 13.1, 12.5, 14.8)\,\mu\mathrm{s}$, termed the return pulse, which aims to project the first-order momentum mode ($\pm 2\hbar k$) back to the $0\hbar k$ mode. Under ideal noninteracting conditions, after the return pulse $\pm 2\hbar k$ is almost completely restored $0\hbar k$.

In Fig. 5, the scattering halo ratio P_{sc} is plotted as a function of the scattering length a_s ($a_s = 865a_0$, $1330a_0$, $1600a_0$, and $2004a_0$), with the particle number fixed at $N_0 = 1.4 \times 10^4$. The red triangles represent the results obtained after applying the first-order momentum mode lattice shortcut pulse sequence, while the blue squares represent the measurements taken after an additional return pulse sequence. The error bars indicate the standard error of five measurements. The

halo ratio P_{sc} obtained after the first-order momentum mode lattice shortcut pulse sequence (red triangles) is significantly higher than that obtained after the return pulse (blue squares), especially at lower scattering lengths ($865a_0$ and $1330a_0$). However, as the scattering length gradually increases, the in-trap contribution to the scattering halo may become more significant. From Fig. 5, we can draw two preliminary conclusions. First, the scattering halo formed during the TOF stage is larger than that produced during the return pulse stage (especially at low scattering lengths). Second, the larger the scattering length, the more the scattering halo is generated during the pulse loading process, which becomes more significant and cannot be ignored.

However, due to experimental limitations, the halos after the return pulses include not only the in-trap contribution of shortcut pulses, but also that of return pulses, and it is difficult to separately isolate the in-trap component of the shortcut pulse. Several reasons may lead to more halos during return pulses. The first reason is that return pulses are much longer than shortcut pulses, which produces a longer in-trap time. The second reason is that higher-order momentum modes ($\pm 4\hbar k$, $\pm 6\hbar k$, etc.) emerge during the return pulse sequence as its duration accumulates. These modes spatially overlap within the trap, inducing enhanced in-trap collisions. Therefore, the actual in-trap contribution of the shortcut pulse is much smaller than the experimental measurement values represented by the blue points. The current experiment cannot quantitatively determine this on its own and can only provide a qualitative analysis.

To address these limitations, future efforts will focus on advanced simulations integrating lattice dynamics and strong interactions, as well as the design of momentum-resolved detection schemes to disentangle TOF and in-trap contributions.

V. CONCLUSION

In this work, we focus on the impact of interactions on the formation of collisional scattering halos. The experiments reveal that N_{sc} aligns with the 8/5 power-law prediction of perturbation theory solely when the number of total particles is below a specific threshold. However, as a_s and N_0 increase, the deviation of the experimental results from perturbation theory becomes more pronounced. To quantitatively assess the applicability of perturbation theory, we introduce a scattering factor γ and determine its correlation with P_{sc}. Our experiments uncover a universal relationship, indicating $P_{sc} = f(\gamma)$, although the exact functional form still requires further determination, it offers a line of thought for delving into the general theory of scattering halos. We simulate the formation of scattering halos outside the perturbative regime and discuss the contribution of in-trap dynamics to the scattering halos using return pulse experiments.

In summary, this study not only measures the impact of interactions on collisional scattering halos experimentally, but also provides new insights into the theoretical study of quantum many-body problems in strongly interacting systems.

ACKNOWLEDGMENTS

The authors thank Zekai Chen and Chen Li for their helpful suggestions. This work is supported by the National Natural Science Foundation of China (Grants No. 92365208, and No. 11920101004) and the National Key Research and Development Program of China (Grants No. 2021YFA0718300 and No. 2021YFA1400900).

DATA AVAILABILITY

The data that support the findings of this article are openly available [52].

APPENDIX A: SHORTCUT SEQUENCES

The shortcut method, due to its robustness [21,46,47], is utilized to prepare BEC into target states in an optical lattice. The basic idea of the shortcut method is to continually turn on and off the optical lattice to modulate the particle state, as shown in Fig. 2(b). In our experiment, the initial state $|\psi_i\rangle$ is the ground state of mBEC in a harmonic trap. After several pulses, the final state of particles $|\psi_f\rangle$ is written as

$$|\psi_T\rangle = \prod_{i=1}^{n} \hat{U}_{\text{off}}\left(t_i^{\text{off}}\right)\hat{U}_{\text{on}}\left(t_i^{\text{on}}\right)|\psi_i\rangle, \tag{A1}$$

where n is the number of pulses, $\hat{U}_{\text{on}}$ and $\hat{U}_{\text{off}}$ are the evolution operators of the particle state when the optical lattice is on and off, respectively, and t_i^{on} and t_i^{off} are the evolution times of the ith pulse.

Through designing the sequence, we can optimize the final state $|\psi_f\rangle$ to the aimed state $|\psi_a\rangle$. The fidelity is defined by $|\langle\psi_f|\psi_a\rangle|^2$ to describe the loading efficiency. As shown in Table I, in the experiment, the optimized sequence has two pulses to load particles into the $\pm 2\hbar k$ momentum states of 1D optical lattices. The theoretical fidelity is calculated under noninteraction conditions. If interactions are considered, the loading fidelity of the shortcut method decreases somewhat. Although there is a drop, we cannot observe condensates in other momentum states experimentally. Thus we conclude that this method is still valid within the strongly interacting regime.

As shown in Fig. 2(c), the occupation numbers of momentum modes can be precisely controlled by lattice pulses. To study the impact of particle number loss during the lattice loading process on the scattering halo, we designed two additional return lattice pulses that can bring most particles back to the $0\hbar k$ mode before the TOF. The specific pulses and theoretical fidelity are shown in Table II.

APPENDIX B: PERTURBATION THEORY

In this section, we provide a detailed derivation of perturbation theory [Eq.(2)]. This theory works when the number of scattering halo particles is small.

TABLE I. The pulse sequences used to prepare particles into the target state $\pm 2\hbar k$ of the 1D optical lattice with lattice depth $V_0 = 10E_r$.

V_0	t_1^{on}[μs]	t_1^{off}	t_2^{on}	t_2^{off}	Theoretical fidelity
$10E_r$	12.3	6.8	7.1	18.2	99.9%

TABLE II. The shortcut sequences used to return the $0\hbar k$ mode in 1D optical lattices with lattice depth $V_0 = 10E_r$.

V_0	$t_{r_1}^{\text{on}}$[μs]	$t_{r_1}^{\text{off}}$	$t_{r_2}^{\text{on}}$	$t_{r_2}^{\text{off}}$	Theoretical fidelity
$10E_r$	19.3	13.1	12.5	14.8	99.3%

By integrating Eq. (1) over TOF time t, we obtain

$$N_{\text{sc}} = 2\sigma v \int dt \left[\int d\vec{r}\, n_+(\vec{r},t) n_-(\vec{r},t) \right], \tag{B1}$$

where $n_\pm(\vec{r},t) \approx n_\pm(\vec{r} \mp \frac{1}{2}\vec{v}t, 0)$. The initial densities of the momentum components $\pm 2\hbar k$, $n_+(\vec{r},0)$, and $n_-(\vec{r},0)$, satisfy the following Eq. (B2):

$$n_+(\vec{r},0) = n_-(\vec{r},0) = \frac{N_0}{2}\phi(\vec{r}/R), \tag{B2}$$

where $\phi(\vec{r}/R)$ is the Thomas-Fermi distribution, and its corresponding expression is

$$\phi(\vec{r}/R) = \text{Max}\left\{ \frac{15}{8\pi R^3}\left[1 - \left(\frac{\omega_x x}{\overline{\omega} R}\right)^2 - \left(\frac{\omega_y y}{\overline{\omega} R}\right)^2 - \left(\frac{\omega_z z}{\overline{\omega} R}\right)^2 \right], 0 \right\}. \tag{B3}$$

The Thomas-Fermi radius R is given by Eq. (3). For any real numbers a and b, the function $\text{Max}\{a,b\}$ is equal to the larger one of a and b.

Note $\vec{\rho} = \frac{\vec{r}}{R}$, $\tau\hat{e}_v = \frac{t}{2R}\vec{v}$, Eq. (B1) can be rewritten as

$$\begin{aligned} N_{\text{sc}} &= 2\sigma v \int dt \left[\int d\vec{r}\, n_+(\vec{r},t) n_-(\vec{r},t) \right] \\ &= 4\sigma \int d\left(\frac{1}{2}vt\right) \left[\int d\vec{r}\, n_+\left(\vec{r} - \frac{1}{2}\vec{v}t, 0\right) n_-\left(\vec{r} + \frac{1}{2}\vec{v}t, 0\right) \right] \\ &= 4\sigma R \int d\tau \left[\int d\vec{r}\, n_+(\vec{r} - \tau R\hat{e}_v) n_-(\vec{r} + \tau R\hat{e}_v) \right] \\ &= \frac{\sigma N_0^2}{R^2} \int d\tau \left[\int d\vec{\rho}\, \phi^2(\vec{\rho} - \tau\hat{e}_v)\phi^2(\vec{\rho} + \tau\hat{e}_v) \right] \\ &= 8\pi\epsilon \left(\frac{a_s N_0}{R}\right)^2. \end{aligned} \tag{B4}$$

Among them, the value of ϵ satisfies

$$\epsilon = \int d\tau \left[\int d\vec{\rho}\phi^2(\vec{\rho} - \tau\hat{e}_v)\phi^2(\vec{\rho} + \tau\hat{e}_v) \right]. \tag{B5}$$

The unit vector of the separation velocity $\vec{v}$ direction $\hat{e}_v = \cos(\pi/4)\hat{e}_x + \sin(\pi/4)\hat{e}_y$. The trapping frequencies are $(\omega_x, \omega_y, \omega_z) = 2\pi \times (39.5, 200, 200)$ Hz, and the mean trapping frequency $\overline{\omega} \approx 2\pi \times 116.5$ Hz. The value of ϵ is obtained by numerical integration of Eq. (B5), and the result is 0.102.

[1] J. Weiner, V. S. Bagnato, S. Zilio, and P. S. Julienne, Rev. Mod. Phys. **71**, 1 (1999).

[2] S. S. Hodgman, R. I. Khakimov, R. J. Lewis-Swan, A. G. Truscott, and K. V. Kheruntsyan, Phys. Rev. Lett. **118**, 240402 (2017).

[3] T. Schweigler, V. Kasper, S. Erne, I. Mazets, B. Rauer, F. Cataldini, T. Langen, T. Gasenzer, J. Berges, and J. Schmiedmayer, Nature (London) **545**, 323 (2017).

[4] E. A. Donley, N. R. Claussen, S. T. Thompson, and C. E. Wieman, Nature (London) **417**, 529 (2002).

[5] C. A. Regal, C. Ticknor, J. L. Bohn, and D. S. Jin, Nature (London) **424**, 47 (2003).

[6] M. W. Zwierlein, C. A. Stan, C. H. Schunck, S. M. F. Raupach, A. J. Kerman, and W. Ketterle, Phys. Rev. Lett. **92**, 120403 (2004).

[7] M. Greiner, C. A. Regal, and D. S. Jin, Nature (London) **426**, 537 (2003).

[8] S. Jochim, M. Bartenstein, A. Altmeyer, G. Hendl, S. Riedl, C. Chin, J. H. Denschlag, and R. Grimm, Science **302**, 2101 (2003).

[9] D. S. Petrov, C. Salomon, and G. V. Shlyapnikov, Phys. Rev. Lett. **93**, 090404 (2004).

[10] C. R. Monroe, E. A. Cornell, C. A. Sackett, C. J. Myatt, and C. E. Wieman, Phys. Rev. Lett. **70**, 414 (1993).

[11] P. Ziń, J. Chwedeńczuk, A. Veitia, K. Rzążewski, and M. Trippenbach, Phys. Rev. Lett. **94**, 200401 (2005).

[12] A. P. Chikkatur, A. Görlitz, D. M. Stamper-Kurn, S. Inouye, S. Gupta, and W. Ketterle, Phys. Rev. Lett. **85**, 483 (2000).

[13] A. Tenart, C. Carcy, H. Cayla, T. Bourdel, M. Mancini, and D. Clément, Phys. Rev. Res. **2**, 013017 (2020).

[14] F. Gerbier, S. Trotzky, S. Fölling, U. Schnorrberger, J. D. Thompson, A. Widera, I. Bloch, L. Pollet, M. Troyer, B. Capogrosso-Sansone, N. V. Prokof'ev, and B. V. Svistunov, Phys. Rev. Lett. **101**, 155303 (2008).

[15] Y. B. Band, M. Trippenbach, J. P. Burke, and P. S. Julienne, Phys. Rev. Lett. **84**, 5462 (2000).

[16] P. Ziń, J. Chwedeńczuk, and M. Trippenbach, Phys. Rev. A **73**, 033602 (2006).

[17] S. Dimopoulos, P. W. Graham, J. M. Hogan, and M. A. Kasevich, Phys. Rev. D **78**, 042003 (2008).

[18] D.-I. Choi and Q. Niu, Phys. Rev. Lett. **82**, 2022 (1999).

[19] J. H. Denschlag, J. E. Simsarian, H. Häffner, C. McKenzie, A. Browaeys, D. Cho, K. Helmerson, S. L. Rolston, and W. D. Phillips, J. Phys. B: At. Mol. Opt. Phys. **35**, 3095 (2002).

[20] C. Wu, W. V. Liu, J. Moore, and S. D. Sarma, Phys. Rev. Lett. **97**, 190406 (2006).

[21] L. Niu, S. Jin, X. Chen, X. Li, and X. Zhou, Phys. Rev. Lett. **121**, 265301 (2018).

[22] C. Wu, D. Bergman, L. Balents, and S. D. Sarma, Phys. Rev. Lett. **99**, 070401 (2007).

[23] X. Guo, Z. Yu, F. Wei, S. Jin, X. Chen, X. Li, X. Zhang, and X. Zhou, Sci. Bull. **67**, 2291 (2022).

[24] X. Dong, S. Jin, H. Shui, P. Peng, and X. Zhou, Chin. Phys. B **30**, 014210 (2021).

[25] D. Hu, L. Niu, S. Jin, X. Chen, G. Dong, J. Schmiedmayer, and X. Zhou, Commun. Phys. **1**, 29 (2018).

[26] H. Shui, S. Jin, Z. Li, F. Wei, X. Chen, X. Li, and X. Zhou, Phys. Rev. A **104**, L060601 (2021).
[27] I. Bloch, J. Dalibard, and S. Nascimbène, Nat. Phys. **8**, 267 (2012).
[28] Z. Yu, J. Tian, P. Peng, D. Mao, X. Chen, and X. Zhou, Phys. Rev. A **107**, 023303 (2023).
[29] H. Shui, C.-K. Lai, Z. Yu, J. Tian, C. Wu, X. Chen, and X. Zhou, Opt. Express **31**, 26599 (2023).
[30] R. Jannin, P. Cladé, and S. Guellati-Khélifa, Phys. Rev. A **92**, 013616 (2015).
[31] N. R. Thomas, N. Kjærgaard, P. S. Julienne, and A. C. Wilson, Phys. Rev. Lett. **93**, 173201 (2004).
[32] C. Buggle, J. Léonard, W. von Klitzing, and J. T. M. Walraven, Phys. Rev. Lett. **93**, 173202 (2004).
[33] N. Q. Burdick, A. G. Sykes, Y. Tang, and B. L. Lev, New J. Phys. **18**, 113004 (2016).
[34] R. Thomas, M. Chilcott, C. Chisholm, A. B. Deb, M. Horvath, B. J. Sawyer, and N. Kjærgaard, J. Phys.: Conf. Ser. **875**, 012007 (2017).
[35] R. Chang, Q. Bouton, H. Cayla, C. Qu, A. Aspect, C. I. Westbrook, and D. Clément, Phys. Rev. Lett. **117**, 235303 (2016).
[36] R. Thomas, M. Chilcott, E. Tiesinga, A. B. Deb, and N. Kjærgaard, Nat. Commun. **9**, 4895 (2018).
[37] D. K. Shin, B. M. Henson, S. S. Hodgman, T. Wasak, J. Chwedeńczuk, and A. G. Truscott, Nat. Commun. **10**, 4447 (2019).
[38] R. I. Khakimov, B. M. Henson, D. K. Shin, S. S. Hodgman, R. G. Dall, K. G. H. Baldwin, and A. G. Truscott, Nature (London) **540**, 100 (2016).
[39] S. Hofferberth, I. Lesanovsky, T. Schumm, A. Imambekov, V. Gritsev, E. Demler, and J. Schmiedmayer, Nat. Phys. **4**, 489 (2008).
[40] N. Katz, E. Rowen, R. Ozeri, and N. Davidson, Phys. Rev. Lett. **95**, 220403 (2005).
[41] C. Li, Q. Liang, P. Paranjape, R. G. Wu, and J. Schmiedmayer, Phys. Rev. Res. **6**, 023217 (2024).
[42] C. Chin, R. Grimm, P. Julienne, and E. Tiesinga, Rev. Mod. Phys. **82**, 1225 (2010).
[43] S. Kotochigova, Rep. Prog. Phys. **77**, 093901 (2014).
[44] P. Courteille, R. S. Freeland, D. J. Heinzen, F. A. van Abeelen, and B. J. Verhaar, Phys. Rev. Lett. **81**, 69 (1998).
[45] M. Bartenstein, A. Altmeyer, S. Riedl, R. Geursen, S. Jochim, C. Chin, J. H. Denschlag, R. Grimm, A. Simoni, E. Tiesinga, C. J. Williams, and P. S. Julienne, Phys. Rev. Lett. **94**, 103201 (2005).
[46] X. Zhou, S. Jin, and J. Schmiedmayer, New J. Phys. **20**, 055005 (2018).
[47] Y. Zhai, X. Yue, Y. Wu, X. Chen, P. Zhang, and X. Zhou, Phys. Rev. A **87**, 063638 (2013).
[48] F. Wei, Z. Zhang, Y. Chen, H. Shui, Y. Liang, C. Li, and X. Zhou, Phys. Rev. A **109**, 043313 (2024).
[49] G. Chatelain, N. Dupont, M. Arnal, V. Brunaud, J. Billy, B. Peaudecerf, P. Schlagheck, and D. Guéry-Odelin, New J. Phys. **22**, 123032 (2020).
[50] Q. Liang, C. Li, S. Erne, P. Paranjape, R. Wu, and J. Schmiedmayer, SciPost Phys. **12**, 154 (2022).
[51] C. Li, T. Zhou, I. Mazets, H.-P. Stimming, F. S. Møller, Z. Zhu, Y. Zhai, W. Xiong, X. Zhou, X. Chen, and J. Schmiedmayer, SciPost Phys. **9**, 058 (2020).
[52] Z. Zhang and Y. Chen (2025), doi:10.17605/OSF.IO/YK573.